International Astronautical Congress, Antalya, Türkiye, 5-9 October 2026.

IAC-26-C1-1-7-x107032

Dioscuri: A Dual-Solar-Array Cooperative Momentum Unloading System

Changgang Zheng[a b]*, **Jianxin Guo**[c], **Liang Zhou**[c], **Guoqi Zhang**[c], **Jionghui Li**[a], **Luyuan Wang**[a], **Jinjun Zheng**[d]

[a] *Institute of Spacecraft System Engineering, Beijing, China*
[b] *Nanjing University, Nanjing, China*
[c] *Beijing Institute of Control Engineering, Beijing, China*
[d] *Institute of Telecommunication and Navigation Satellites, Beijing, China*

* Corresponding Author

Abstract

During long-term operations in lunar orbit, spacecraft are inevitably subjected to persistent environmental disturbance torques, leading to the accumulation of angular momentum and eventual saturation of reaction wheels. Unlike Earth-orbiting spacecraft, lunar orbiters cannot rely on magnetic torquers due to the absence of a global magnetic field. Conventional thruster-based momentum unloading introduces propellant consumption and degrades orbit prediction accuracy by disturbing the spacecraft center-of-mass dynamics. To address this challenge, we propose Dioscuri, a cooperative dual-solar-array momentum unloading attitude control strategy based on solar radiation pressure. The system continuously monitors the accumulated external disturbance torque acting on the reaction wheels and triggers momentum unloading once a predefined threshold is reached. By dynamically planning the coordinated rotational profiles of the dual solar arrays while maintaining a constant effective illuminated area, a controllable unloading torque is generated through the intentional deviation of solar radiation pressure vectors from the two arrays. This actively counteracts the accumulated disturbance momentum and prevents reaction wheel saturation without the use of thrusters. The core of this system lies in establishing an accurate attitude dynamics model tailored to orbital characteristics, designing a momentum accumulation-based unloading trigger mechanism, and developing a cooperative dual-solar-array trajectory generation algorithm to precisely match unloading timing and torque output. Simulations demonstrate that Dioscuri effectively mitigates reaction wheel saturation risks and enables continuous reaction wheel operation without using thrusters. The proposed strategy significantly reduces propellant consumption and improves orbit prediction accuracy, offering a low-consumption and practical attitude control solution for long-lifetime lunar and deep-space missions.

Keywords: Reaction-Wheel Momentum Unloading, Solar Radiation Pressure, Dual Solar Arrays, Three-Axis Attitude Control, Lunar and Deep-Space Missions

1. Introduction

Lunar exploration has emerged as a major focus of international space activities [1–3]. Driven by scientific exploration and potential utilization of lunar resources, the Moon, as Earth's closest extraterrestrial body with significant resource potential, has attracted increasing attention. Lunar regolith contains helium-3 and other valuable resources, while permanently shadowed regions near the lunar poles preserve abundant water ice [4–6]. Meanwhile, the Moon lacks an atmosphere, a global magnetic field, and significant geological activity, allowing it to preserve primordial records of the Solar System accumulated over 4.5 billion years [7, 8]. The Moon preserves important information about the early Solar System [9], making it a unique platform for studying planetary formation and evolution.

Major space agencies and countries have launched ambitious lunar exploration programs. The United States is promoting the Artemis program to enable human return to the Moon, explore the lunar south polar region, and establish sustainable lunar infrastructure [3, 10, 11]. China is advancing the Chang'e program and its crewed lunar exploration program toward south-polar exploration, human lunar missions, and the planned International Lunar Research Station [2, 12, 13]. Meanwhile, Russia, ESA, Japan, India, and the Republic of Korea are also pursuing long-term lunar exploration initiatives [1, 14]. These efforts indicate that lunar exploration is evolving from isolated scientific missions toward sustained operations requiring advanced transportation, communication, navigation, remote sensing, and infrastructure capabilities.

Beyond advances in heavy-lift launch systems, Earth–Moon transportation, long-duration lunar habitation and life support, and in-situ resource utilization, the realization of these long-term lunar missions also relies on fundamental spacecraft technologies, including lunar communication, navigation, remote sensing constellations, and high-precision orbit and attitude control [15–19]. Although such technologies may appear conventional, the substantial environmental differences between Earth orbit and the Earth–Moon system make many conventional spacecraft approaches inapplicable. A representative example is momentum unloading using magnetic torquers, which is unavailable in lunar and deep-space environments due to the lack of a global magnetic field. For long-life service spacecraft requiring high orbit-prediction accuracy, such as navigation, remote-sensing, and TT&C satellites, trajectory perturbations and additional propellant consumption during long-term operations should be minimized. At the same time, although spacecraft solar arrays absorb solar radiation for power generation, they are inevitably subjected to solar radiation pressure. Because the center of pressure generally does not coincide with the center of mass, solar radiation pressure generates persistent disturbance torques that accumulate angular momentum and may eventually saturate the reaction wheels of a zero-momentum attitude control system.

Conversely, if the solar-radiation pressure acting on solar arrays can be properly controlled, it can generate controllable attitude control torque and assist reaction-wheel disturbance torque unloading in zero-momentum attitude control systems. The underlying idea has been explored previously. Early studies investigated solar-array-based attitude control for large geostationary satellites rather than momentum unloading. In 1985, J. Lievre proposed such a concept [18], and in 1992, Ruth Azor extended solar-array attitude control to bias-momentum geostationary satellites [20]. However, these methods required auxiliary flaps attached to the solar arrays. By independently modulating solar illumination on the auxiliary surfaces of the north and south arrays, they generated control torque about only a single body axis, typically the Z- or X-axis. More recent studies have primarily focused on spacecraft equipped with large membrane solar sails, where attitude control is achieved during deep-space flight by actively changing sail angles or moving the spacecraft center of mass. Such techniques, however, are not directly applicable to conventional spacecraft solar arrays, whose primary function is electrical power generation rather than attitude control.

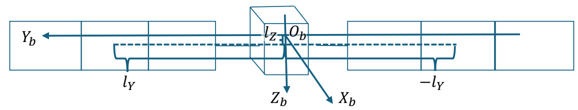

Fig. 1: Schematic of eccentrically mounted solar arrays.

Under typical conditions, as shown in Fig. 1, a spacecraft is equipped with two solar arrays stowed on the spacecraft Y-panel. After on-orbit deployment, the spacecraft attitude is controlled such that the solar vector remains perpendicular to the spacecraft Y-axis, and the solar arrays rotate about the Y-axis to align their surface normals with the solar vector, thereby maximizing electrical power generation through solar tracking. Although spacecraft operational attitudes may vary depending on mission requirements, these geometric constraints generally remain applicable.

Under these constraints, this paper focuses on a general spacecraft configuration equipped with dual solar arrays. We investigate three-axis decoupled disturbance torque unloading using only existing conventional solar arrays without auxiliary flaps. The proposed method is applicable to lunar and deep-space missions, where magnetic torquer-based momentum unloading is unavailable and thruster-based unloading is undesirable due to the induced perturbations to spacecraft trajectory and additional propellant consumption.

2. System Modeling

2.1 Solar-Array Torque Model

A local body-fixed coordinate system is established with its origin at the spacecraft center of mass. The Y_b-axis is normal to the ecliptic plane, the X_b-axis is approximately along the spacecraft's velocity direction, and the Z_b-axis completes the right-handed orthonormal frame. From the spacecraft perspective, the Sun undergoes approximately circular motion around O_b in the local X_bZ_b plane. The Earth also remains approximately in this plane with a small out-of-plane oscillation. At the same time, the Moon moves in the local Y_bZ_b plane, providing the lunar-pointing reference for the subsequent unloading strategy.

The spacecraft is equipped with two symmetrically mounted solar arrays on the Y-panel, and each array has one rotational degree of freedom with its rotation axis parallel to the spacecraft Y_b-axis. In practice, non-ideal mounting conditions may occur, and installation errors are typically compensated by balancing masses on the spacecraft bus. In this work, a residual eccentricity component along the Z_b-axis is intentionally retained. Specifically, if the projection of the solar-array rotation axis onto the spacecraft $X_b Z_b$ plane is denoted as $[0, l_z]$, the centroid positions of the two deployed solar arrays are expressed as $[0, l_Y, l_z]^T$ and $[0, -l_Y, l_z]^T$, respectively. Therefore, each solar array can be modeled as a dual-eccentricity structure with eccentricities l_Y and l_Z, as illustrated in Fig. 1.

The spacecraft velocity vector in the Moon-centered ecliptic inertial frame is $\boldsymbol{v}_I = [v_{XI}, v_{YI}, v_{ZI}]^T$, where

$$\begin{cases} v_{XI} = \dfrac{\mu_m e \sin f}{h}(\cos\Omega\cos\mu - \sin\Omega\sin\mu\cos i) \\ \quad - \dfrac{h}{r}(\cos\Omega\sin\mu + \sin\Omega\cos\mu\cos i), \\ v_{YI} = \dfrac{\mu_m e \sin f}{h}(\sin\Omega\cos\mu + \cos\Omega\sin\mu\cos i) \\ \quad - \dfrac{h}{r}(\sin\Omega\sin\mu - \cos\Omega\cos\mu\cos i), \\ v_{ZI} = \dfrac{\mu_m e \sin f}{h}\sin\mu\sin i + \dfrac{h}{r}\cos\mu\sin i. \end{cases} \tag{1}$$

In this equation, a is the orbital semimajor axis, e is the eccentricity, i is the inclination, Ω is the right ascension of the ascending node, ω is the argument of pericenter, E is the eccentric anomaly, and f is the true anomaly. The auxiliary variables are defined as $r = a(1 - e\cos E)$, $\mu = \omega + f$, and $h = \sqrt{\mu_m a(1 - e^2)}$, where μ_m denotes the lunar gravitational constant.

The unit vector of the spacecraft velocity axis expressed in the inertial frame is defined as

$$\boldsymbol{e}_{v,I} = \frac{\boldsymbol{v}_I}{\|\boldsymbol{v}_I\|}. \tag{2}$$

The basis vectors of the spacecraft body axes in the inertial frame are given by

$$\boldsymbol{e}_{Yb,I} = [0, 1, 0]^{\mathrm{T}},\ \boldsymbol{e}_{Zb,I} = \boldsymbol{e}_{v,I} \times \boldsymbol{e}_{Yb,I}, \tag{3}$$

and the $\boldsymbol{e}_{Xb,I}$ can be generated via $\boldsymbol{e}_{Yb,I}$ and $\boldsymbol{e}_{Zb,I}$.

The transformation matrix from the inertial frame to the spacecraft body-fixed frame is defined as

$$\mathbf{T}_{I\to b} = \left[\boldsymbol{e}_{Xb,I}, \boldsymbol{e}_{Yb,I}, \boldsymbol{e}_{Zb,I}\right]^{\mathrm{T}}. \tag{4}$$

The unit vector of the solar radiation direction in the Moon-centered ecliptic inertial frame is defined as

$$\boldsymbol{e}_s = [e_{sx}, 0, e_{sz}]^{\mathrm{T}},\ \boldsymbol{e}_{sb} = \mathbf{T}_{I\to b}\boldsymbol{e}_s, \tag{5}$$

where $\boldsymbol{e}_{sb}$ denotes the solar unit vector expressed in the spacecraft body-fixed frame.

When disturbance torque unloading is not performed, the surface normal vector of each solar array is maintained opposite to the solar incident direction. During unloading, each solar array is rotated about the Y_b-axis by a small offset angle α relative to the nominal sun-pointing attitude according to the right-hand rule, where $|\alpha| \ll 1\ \mathrm{rad}$. The unit normal vector of the solar-array surface expressed in the spacecraft body-fixed frame is therefore given by

$$\boldsymbol{e}_{sw} = \begin{bmatrix} -\alpha e_{sz} \\ 0 \\ +\alpha e_{sx} \end{bmatrix} = \begin{bmatrix} e_{swx} \\ 0 \\ e_{swz} \end{bmatrix}. \tag{6}$$

The solar-radiation-pressure force acting on a solar array is given by

$$\boldsymbol{F}_b = K_1 \boldsymbol{e}_{sb} + K_2 \boldsymbol{e}_{sw} = K_1 \begin{bmatrix} e_{sx} \\ 0 \\ e_{sz} \end{bmatrix} + K_2 \begin{bmatrix} -\alpha e_{sz} \\ 0 \\ \alpha e_{sx} \end{bmatrix} = \begin{bmatrix} F_x \\ 0 \\ F_z \end{bmatrix}. \tag{7}$$

K_1 and K_2 are the solar-radiation-pressure coefficients, which are defined as

$$K_1 = P_0 S C_a \cos\alpha,\ K_2 = P_0 S \left(2C_r \cos^2\alpha + \frac{2C_d}{3}\cos\alpha\right). \tag{8}$$

$P_0 = 4.56\times10^{-6}\ \mathrm{N/m^2}$ is the solar radiation pressure, S is the area of a single solar array, C_a is the absorptivity, C_d is the diffuse reflectivity, and C_r is the specular reflectivity.

For a small offset angle α, the corresponding approximations of K_1 and K_2 is given by

$$K_1 = P_0 S C_a,\ K_2 = 2P_0 S\left(C_r + \frac{C_d}{3}\right). \tag{9}$$

In general, the centroid of a solar array is assumed to coincide with its center of pressure. Therefore, the solar-radiation-pressure torque generated about the spacecraft center of mass can be expressed as

$$\boldsymbol{M}_{sa} = \boldsymbol{r}_c \times \boldsymbol{F}_b = \begin{bmatrix} 0 \\ l_Y \\ l_Z \end{bmatrix} \times \begin{bmatrix} F_x \\ 0 \\ F_z \end{bmatrix} = \begin{bmatrix} l_Y F_z \\ l_Z F_x \\ -l_Y F_x \end{bmatrix}. \tag{10}$$

If the $+Y$ and $-Y$ arrays rotate by equal but opposite angles, the torques generated by two arrays are given by

$$\boldsymbol{M}_{+Y}(\alpha) = \begin{bmatrix} l_Y(K_1 e_{sz} + K_2\alpha e_{sx}) \\ l_Z(K_1 e_{sx} - K_2\alpha e_{sz}) \\ -l_Y(K_1 e_{sx} - K_2\alpha e_{sz}) \end{bmatrix}, \tag{11}$$

$$\boldsymbol{M}_{-Y}(\alpha) = \begin{bmatrix} -l_Y(K_1 e_{sz} - K_2\alpha e_{sx}) \\ l_Z(K_1 e_{sx} + K_2\alpha e_{sz}) \\ l_Y(K_1 e_{sx} + K_2\alpha e_{sz}) \end{bmatrix}. \tag{12}$$

The combined torque generated by the two arrays is expressed as

$$\boldsymbol{M}_{sa}(\alpha) = \boldsymbol{M}_{+Y}(\alpha) + \boldsymbol{M}_{-Y}(\alpha) = \begin{bmatrix} 2l_Y K_2 \alpha e_{sx} \\ 2l_Z K_1 e_{sx} \\ 2l_Y K_2 \alpha e_{sz} \end{bmatrix}. \quad (13)$$

It can be seen that opposite small-angle rotations of the two arrays can generate unloading torques along all three spacecraft axes. However, the three torque components are strongly coupled, and a decoupling strategy is required.

If the $+Y$ and $-Y$ arrays rotate by the same angle, the combined torque is expressed as

$$\boldsymbol{M}_{sa}(\alpha) = \boldsymbol{M}_{+Y}(\alpha)+\boldsymbol{M}_{-Y}(\alpha) = \begin{bmatrix} 0 \\ 2l_Z(K_1 e_{sx} - K_2 \alpha e_{sz}) \\ 0 \end{bmatrix}. \quad (14)$$

This indicates that identical rotation angles of the two arrays can independently generate an unloading torque about the Y-axis without three-axis coupling.

If the $+Y$ solar array rotates by a nonzero angle while the $-Y$ array remains fixed, the resulting torque is given by

$$\boldsymbol{M}_{sa}(\alpha) = \boldsymbol{M}_{+Y}(\alpha)+\boldsymbol{M}_{-Y}(0) = \begin{bmatrix} l_Y K_2 \alpha e_{sx} \\ l_Z(2K_1 e_{sx} - K_2 \alpha e_{sz}) \\ l_Y K_2 \alpha e_{sz} \end{bmatrix}. \quad (15)$$

In this case, coupling among the three torque components remains, motivating the development of a decoupling strategy.

2.2 Reaction-Wheel Momentum Unloading

The spacecraft is equipped with four reaction wheels and adopts a zero-momentum attitude control configuration. The total angular momentum of the spacecraft system is maintained as

$$\boldsymbol{H}_{\text{total}} = \mathbf{I}\boldsymbol{\omega} + \boldsymbol{h}_w = \mathbf{0}, \quad (16)$$

where $\boldsymbol{\omega}$ is the spacecraft angular velocity vector with respect to the inertial frame, $\boldsymbol{h}_w$ is the reaction-wheel angular momentum, and $\mathbf{I}$ is the spacecraft inertia matrix.

In the spacecraft body-fixed frame, the rigid-body attitude dynamics are described by the Euler equation

$$\mathbf{I}\dot{\omega} + \boldsymbol{\omega} \times (\mathbf{I}\boldsymbol{\omega} + \boldsymbol{h}_w) = \boldsymbol{M}_{\text{env}} + \boldsymbol{M}_c + \boldsymbol{M}_{sa}(\alpha). \quad (17)$$

In this equation, $\boldsymbol{M}_{\text{env}}$ denotes the environmental disturbance torque, which consists of the secular component $\boldsymbol{M}_{\text{sec}}$ and the periodic component $\boldsymbol{M}_{\text{per}}$. The reaction wheels generate the control torque $\boldsymbol{M}_c$, which satisfies $\boldsymbol{M}_c = -\dot{\boldsymbol{h}}_w$. The term $\boldsymbol{M}_{sa}(\alpha)$ represents the additional control torque generated by actively deflecting the eccentrically mounted solar arrays by an angle α.

For a spacecraft operating in lunar orbit, the dominant long-period disturbance torques arise from the torque induced by imperfect installation of the two solar arrays and the third-body gravity-gradient torques induced by the Sun and the Earth. These disturbance torques are typically on the order of $5 \times 10^{-6}\,\mathrm{N \cdot m}$. Without disturbance-torque unloading, the reaction wheels would reach saturation in approximately 30 days.

When the spacecraft attitude $\boldsymbol{\phi}$ remains relatively stable and no rapid large-angle maneuver is required, the attitude dynamics can be linearized under the small-angle assumption. The spacecraft angular velocity can then be approximated as

$$\boldsymbol{\omega} \approx \dot{\boldsymbol{\phi}} + \boldsymbol{\omega}_0, \quad (18)$$

where $\boldsymbol{\omega}_0$ denotes the orbital angular velocity vector. By neglecting higher-order small terms associated with $\boldsymbol{\omega}\times(\cdot)$, the linearized attitude dynamics become

$$\mathbf{I}\ddot{\boldsymbol{\phi}} + \dot{\boldsymbol{h}}_w = \boldsymbol{M}_{\text{env}} + \boldsymbol{M}_{sa}(\alpha). \quad (19)$$

For a zero-momentum attitude control system, the control objective is to maintain the average variation rate of the total spacecraft angular momentum at zero. Therefore,

$$\frac{1}{T}\int_0^T \dot{\boldsymbol{h}}_w \,\mathrm{d}t = \boldsymbol{M}_{\text{sec}} + \frac{1}{T}\int_0^T \boldsymbol{M}_{sa}(\alpha)\,\mathrm{d}t. \quad (20)$$

Considering that the dominant periodic components of the disturbance torque are the orbital-period and draconic-period components, with the orbital-period component being dominant, the averaging interval T is generally selected as one orbital period.

If reaction wheels are used primarily to compensate for periodic disturbances $\boldsymbol{M}_{\text{per}}$, the control torque generated by eccentrically mounted solar arrays should compensate for the secular disturbance torque $\boldsymbol{M}_{\text{sec}}$, such that

$$\frac{1}{T}\int_0^T \dot{\boldsymbol{h}}_w \,\mathrm{d}t \approx \mathbf{0}. \quad (21)$$

During on-orbit operation, the Sun undergoes approximately circular motion around O_b in the local $X_b Z_b$ plane. Over one orbital period, the integral of the solar unit vector expressed in the spacecraft body-fixed frame is approximately zero. Therefore, the eccentrically mounted solar arrays cannot generate a net unloading torque through constant-angle deflection. Time-varying control based on the solar-vector direction $\boldsymbol{e}_{sb}$ is required to generate effective unloading torques and achieve three-axis torque decoupling.

Table 1: Dual-Solar-Array Momentum Unloading Control Logic

Region	Deflection Configuration	Dominant Lever Arm	Control Torque	Primary Objective
I or III (G1)	$\delta_A = \alpha,\ \delta_B = -\alpha$	l_Y dominant	M_Z	Reaction-wheel momentum unloading along the Z-axis, with coupled X/Y torques cancelled.
II or IV (G2)	Region II: $\delta_A = \alpha,\ \delta_B = -\alpha$ Region IV: $\delta_A = \alpha,\ \delta_B = \alpha$ or Region II: $\delta_A = \alpha,\ \delta_B = \alpha$ Region IV: $\delta_A = \alpha,\ \delta_B = -\alpha$	l_Y dominant, l_Z compensated	M_X	Reaction-wheel momentum unloading along the X-axis, with coupled Y/Z torques compensated through regional control.
II or IV (G3)	$\delta_A = \alpha,\ \delta_B = \alpha$ or $\delta_A = -\alpha,\ \delta_B = -\alpha$	l_Z dominant	M_Y	Reaction-wheel momentum unloading along the Y-axis.

For a circular orbit, the angle between the solar unit vector $\boldsymbol{e}_{sb}$ and the spacecraft $+Z_b$-axis is defined as

$$\theta_{zs} = \mathrm{mod}\left[\mathrm{atan2}(e_{sx}, e_{sz}),\ 2\pi\right]. \tag{22}$$

The control space is divided into four regions according to the range of θ_{zs}:

$$\begin{cases} \mathrm{I}: & -45^\circ < \theta_{zs} < 45^\circ, \\ \mathrm{II}: & 45^\circ < \theta_{zs} < 135^\circ, \\ \mathrm{III}: & 135^\circ < \theta_{zs} < 225^\circ, \\ \mathrm{IV}: & 225^\circ < \theta_{zs} < 315^\circ. \end{cases} \tag{23}$$

By commanding different deflection angles of the two solar arrays in different regions, three-axis control torques can be generated, as summarized in Table 1.

3. Momentum Unloading Strategy

Based on the solar-array torque model and reaction-wheel momentum dynamics established above, a dual-solar-array momentum unloading strategy is developed. The proposed unloading strategy is implemented through a region-dependent control process and is summarized in six phases.

3.1 On-Orbit Implementation Strategy

Phase 1: On-orbit preprocessing and model calibration (after orbit insertion and attitude stabilization).

Step 1-1: Establish the nominal attitude state. After orbit insertion, the spacecraft attitude-control loop maintains the nominal lunar-orbiting attitude, with the X_b-axis aligned with the spacecraft velocity direction, the Y_b-axis perpendicular to the ecliptic plane, and the Z_b-axis pointing toward the lunar center. When the attitude error is reduced below 0.1° and the reaction wheels operate around the nominal zero-momentum condition, the three-axis reaction-wheel angular momentum and wheel speeds are recorded to establish the initial unloading reference state.

Step 1-2 : On-orbit calibration of the dual-eccen-tricity solar-radiation-pressure model coefficients. Both solar arrays are first returned to the nominal sun-pointing zero-bias position, i.e., $\delta_A = \delta_B = 0$, to ensure optimal power generation and establish a unique baseline state. Then, independent small-angle probing deflections are applied to characterize the array torque response. Specifically, differential test commands $(\delta_A, \delta_B) = (\delta_{\mathrm{test}}, -\delta_{\mathrm{test}})$ and common-mode test commands $(\delta_A, \delta_B) = (\delta_{\mathrm{test}}, \delta_{\mathrm{test}})$ are executed. Based on the measured reaction-wheel momentum variations and the unified dual-eccentricity model described by Eqs. (13) and (14), the SRP model coefficients K_1 and K_2 are estimated. According to the torque-generation characteristics summarized in Table 1, three sets of torque-control coefficients under Regions I–IV and different solar incidence angles are stored in the onboard regional parameter table for accurate region-dependent modeling. The known parameters, including the solar-array area S, optical coefficients (C_a, C_s, and C_d), solar radiation pressure constant P_0, and the dual-eccentricity vector $\boldsymbol{l} = [0, l_Y, l_Z]^{\mathrm{T}}$, are then fixed to construct the unified torque–deflection analytical model.

Step 1-3: Unloading thresholds (activation and deactivation) configuration using a hysteresis criterion. To avoid frequent switching of the solar-array unloading commands, independent activation and deactivation thresholds are defined for each spacecraft axis. When the reaction-wheel momentum exceeds the corresponding activation threshold, the solar-radiation-pressure unloading control for that axis is enabled; when the momentum decreases below the deactivation threshold, the solar arrays return to the nominal zero-bias position and the unloading action is terminated. The hysteresis logic is given as

$$\begin{cases} \text{activate unloading along the corresponding axis,} \\ \qquad |H_i| > H_{\mathrm{th},i}, \quad i \in \{x, y, z\}, \\ \text{return to nominal zero-bias position and stop unloading,} \\ \qquad |H_i| < H_{\mathrm{off},i}, \quad i \in \{x, y, z\}. \end{cases} \tag{24}$$

During lunar shadow passages, when solar radiation pressure becomes unavailable, the solar-radiation-pressure unloading control is directly disabled. The reaction wheels maintain the spacecraft attitude, and the unloading process resumes after eclipse exit when solar-radiation-pressure control becomes available again.

Phase 2: Real-time orbital region identification (executed once per orbital cycle).

Step 2-1: Real-time solar-vector angle calculation. Using the onboard Sun sensor measurements and orbit propagation results, the solar unit vector in the spacecraft body-fixed frame, $\boldsymbol{e}_{sb} = (e_{sx}, e_{sy}, e_{sz})^{\mathrm{T}}$, is determined. The angle between the solar direction and the lunar-pointing Z_b-axis is then calculated as θ_{zs}.

Step 2-2: Region and control-group selection. According to the calculated solar-vector angle θ_{zs}, the onboard controller automatically selects the corresponding control group. When $\theta_{zs} \in [-45°, 45°] \cup [135°, 225°]$, control group G1 is activated. The two solar arrays apply anti-phase deflection, $(\delta_A, \delta_B) = (+\delta, -\delta)$, to achieve pure Z-axis momentum unloading through the Y-direction eccentricity.

When $\theta_{zs} \in [45°, 135°] \cup [225°, 315°]$, control groups G2 and G3 are activated for X- and Y-axis momentum unloading, respectively. For control group G2, Region II adopts anti-phase deflection $(\delta_A, \delta_B) = (+\delta, -\delta)$, while Region IV adopts common-mode deflection $(\delta_A, \delta_B) = (+\delta, +\delta)$, enabling pure X-axis unloading through the Y-direction eccentricity. For control group G3, Region II applies common-mode deflection $(\delta_A, \delta_B) = (+\delta, +\delta)$, whereas Region IV returns both arrays to the zero-deflection position $(\delta_A, \delta_B) = (0, 0)$, enabling pure Y-axis unloading through the Z-direction eccentricity.

Phase 3: Stepwise Z-axis unloading in control group G1 (Regions I and III), using dual-eccentricity decoupling control. The control configuration adopts equal-magnitude and opposite-direction deflections of the two solar arrays, i.e., $(\delta_A, \delta_B) = (\delta, -\delta)$. Regions I and III are independently controlled under this configuration, which exploits the decoupling capability provided by the $l_Y + l_Z$ dual-eccentricity model. Due to the opposite signs of the Y-direction lever arms of the two arrays, the coupled torque about the X-axis is automatically cancelled. Meanwhile, the identical Z-direction lever arms generate torque components with opposite effects, leading to cancellation of the coupled Y-axis torque. Therefore, the resulting control torque satisfies $M_{Xc} \approx 0$ and $M_{Yc} \approx 0$, enabling Z-axis reaction-wheel momentum unloading without disturbing the momentum states along the X- and Y-axes.

Step 3-1: Momentum state monitoring and disturbance torque estimation. The Z-axis reaction-wheel angular momentum H_Z is monitored in real time, and the equivalent disturbance torque is estimated as $M_{dZ} = \dot{H}_Z$. The target solar-radiation-pressure unloading torque is then set to $M_{Zc} = -M_{dZ}$.

Step 3-2: Control deflection angle calculation based on the dual-eccentricity model. A region-dependent control law is adopted to accommodate the coupling characteristics of the dual-eccentricity torque model. When the spacecraft is located in Region I ($\theta_{zs} \in [-45°, 45°]$) or Region III ($\theta_{zs} \in [135°, 225°]$), the solar direction is close to the spacecraft Z_b-axis. After averaging over the corresponding control region, the torque components generated by the l_Y term along the X-axis and by the l_Z term along the Y-axis are approximately cancelled, while the torque component generated by the l_Y term along the Z-axis remains nonzero. Therefore, the required deflection angle δ can be obtained from Eq. (13).

$$\delta = \begin{cases} \delta_{\mathrm{th}}, & \dfrac{-M_{dZ}}{2 l_Y K_2 \int e_{sz}(\theta_{zs}) \, \mathrm{d}\theta_{zs}} \geq \delta_{\mathrm{th}}, \\ \dfrac{-M_{dZ}}{2 l_Y K_2 \int e_{sz}(\theta_{zs}) \, \mathrm{d}\theta_{zs}}, & \text{otherwise.} \end{cases} \tag{25}$$

Step 3-3: SADA deflection execution and closed-loop correction. The $+Y$ solar array is commanded to deflect by $+\delta$, while the $-Y$ solar array is commanded to deflect by $-\delta$. The deflection angle is strictly constrained by $\delta \leq \delta_{\mathrm{th}}$ to maintain the validity of the small-angle approximation and satisfy the power-generation constraint. The reaction-wheel momentum is monitored in closed loop, and the deflection angle δ is adjusted according to the measured variation of H_Z such that $\dot{H}_Z \to 0$. During operation, the decoupling performance is continuously verified by monitoring the X- and Y-axis momentum states, ensuring that no unexpected momentum drift or accumulation occurs under the symmetric anti-phase dual-eccentricity configuration.

Step 3-4: Exit G1 mode. When the exit condition $|H_Z| < H_{\mathrm{off}}$ is satisfied, the control deflection angle δ is smoothly driven back to zero to avoid abrupt torque changes. Both solar arrays return to the nominal sun-pointing position, and the system waits for the next orbital-region transition.

Phase 4: Stepwise X-axis unloading in control group G2 (Regions II and IV), using dual-eccentricity decoupling control. The control configuration adopts coordinated control between Regions II and IV. In Region II, the two solar arrays apply differential deflection with equal magnitude and opposite directions, i.e., $(\delta_A, \delta_B) = (\delta, -\delta)$. In Region IV, common-mode deflection is applied, i.e., $(\delta_A, \delta_B) = (\delta, \delta)$. Through the combined utilization of the l_Y and l_Z eccentricities, the coupled torques generated in Regions II and IV are compensated, enabling decoupled X-axis momentum unloading. In Region II, the opposite Y-direction eccentric contributions of the two arrays cancel the coupled Z-axis torque, while the in-phase Z-direction eccentric contributions introduce a coupled Y-axis torque. In Region IV, the in-phase Z-direction eccentric contributions generate a Y-axis torque with opposite polarity to that produced in Region II, thereby compensating the remaining coupling component. As a result, the resulting control torque satisfies $M_{Yc} \approx 0$ and $M_{Zc} \approx 0$, enabling X-axis reaction-wheel momentum unloading without disturbing the momentum states along the Y- and Z-axes.

Step 4-1: Momentum state monitoring and disturbance torque estimation. The X-axis reaction-wheel angular momentum H_X is monitored in real time, and the equivalent disturbance torque is estimated as $M_{dX} = \dot{H}_X$. The target solar-radiation-pressure unloading torque is then determined as $M_{Xc} = -M_{dX}$.

Step 4-2: Control deflection angle calculation based on the dual-eccentricity model. A region-dependent coordinated control logic is adopted to accommodate the torque-coupling characteristics of the dual-eccentricity model. The required deflection angle is calculated according to Eq. (13), where the equivalent control gain $K_{MX}(\theta_{zs}, l_Y, l_Z)$ is determined by the current solar-vector region and eccentricity parameters. The control relationship can be expressed as

$$-M_{dX} = K_{MX}(\theta_{zs}, l_Y, l_Z)\delta \tag{26}$$

which gives

$$\delta = \frac{-M_{dX}}{K_{MX}(\theta_{zs}, l_Y, l_Z)} = \frac{-M_{dX}}{2l_Y K_2 \int e_{sx}(\theta_{zs})\,\mathrm{d}\theta_{zs}}. \tag{27}$$

When the calculated deflection angle exceeds the allowable limit $\delta \geq \delta_{\mathrm{th}}$, it is saturated at δ_{th} to maintain the validity of the small-angle approximation and satisfy power-generation constraints. This control law enables unloading of both positive and negative X-axis disturbance torques without control blind zones.

Step 4-3: SADA deflection execution and torque compensation. In Region II, solar arrays A and B apply opposite deflections with equal magnitude, generating the desired X-axis control torque through the l_Y eccentricity. The symmetric differential configuration cancels the coupled Z-axis torque introduced by the l_Y term. Meanwhile, the additional coupled Y-axis torque generated by the l_Z eccentricity is compensated in Region IV, where solar arrays A and B apply common-mode deflection to generate an independent counteracting Y-axis torque.

Step 4-4: Closed-loop convergence and exit. When the exit condition $|H_X| < H_{\mathrm{off}}$ is satisfied, the deflection angle δ is smoothly reduced to zero. Both solar arrays return to the nominal sun-pointing position, and the system automatically switches to the corresponding regional control mode.

Phase 5: Stepwise Y-axis unloading in control group G3 (Regions II and IV), using l_Z-eccentricity decoupling control. The control configuration adopts common-mode deflection in Region II, where the two solar arrays apply equal-magnitude and same-direction commands, i.e., $(\delta_A, \delta_B) = (\delta, \delta)$. In Region IV, both arrays return to the nominal sun-pointing position. By exploiting the Z-direction eccentricity and coordinating the control actions between Regions II and IV, the coupled torque components along the X- and Z-axes are canceled, satisfying $M_{Xc} \approx 0$ and $M_{Zc} \approx 0$. Therefore, decoupled unloading of the Y-axis reaction-wheel momentum is achieved.

Step 5-1: Momentum state monitoring and disturbance torque estimation. The Y-axis reaction-wheel angular momentum H_Y is monitored in real time, and the equivalent disturbance torque is estimated as $M_{dY} = \dot{H}_Y$. The target solar-radiation-pressure unloading torque is then determined as $M_{Yc} = -M_{dY}$.

Step 5-2: Control deflection angle calculation based on the eccentricity model. A two-region joint control logic is adopted. When the spacecraft is located in Region II, i.e., $\theta_{zs} \in [45°, 135°]$, or Region IV, i.e., $\theta_{zs} \in [225°, 315°]$, the solar-radiation-pressure torque generated through the Z-direction eccentricity produces the desired Y-axis control torque. Since the two solar arrays apply common-mode deflection, the coupled torque components along the X- and Z-axes are cancelled. Therefore, the required deflection angle can be obtained from Eq. (14).

$$\delta = \begin{cases} \delta_{\mathrm{th}}, & \dfrac{-M_{dY}}{2l_Z K_1 \int e_{sx}(\theta_{zs})\,\mathrm{d}\theta_{zs}} \geq \delta_{\mathrm{th}}, \\ \dfrac{-M_{dY}}{2l_Z K_1 \int e_{sx}(\theta_{zs})\,\mathrm{d}\theta_{zs}}, & \text{otherwise.} \end{cases} \tag{28}$$

Step 5-3: SADA deflection execution and closed-loop correction. In Region II, both solar arrays are commanded to deflect by $+\delta$, with the constraint $\delta \leq \delta_{\text{th}}$ to maintain the validity of the small-angle approximation and satisfy power-generation constraints. In Region IV, both arrays return to the nominal sun-pointing position. The reaction-wheel momentum is monitored in closed loop, and the deflection angle δ is adjusted based on the l_Z eccentricity such that $\dot{H}_Y \to 0$. The decoupling performance is verified by ensuring that the coupled torque components satisfy $M_{Xc} \approx 0$ and $M_{Zc} \approx 0$, without unexpected momentum accumulation along the X- and Z-axes.

Step 5-4: Exit G3 mode. When the exit condition $|H_Y| < H_{\text{off}}$ is satisfied, the control deflection angle δ is smoothly reduced to zero. Both solar arrays return to the nominal sun-pointing position, and the system waits for the next orbital-region transition.

Phase 6: Inter-region transition, eclipse contingency handling, and long-term autonomous operation.

Step 6-1: Smooth transition between adjacent regions. When the solar-vector angle crosses the regional boundaries at $45°$, $135°$, $225°$, and $315°$, a ramped transition strategy is adopted for the deflection angle δ to avoid abrupt torque variations and maintain attitude stability.

Step 6-2: Lunar-eclipse and shadow-region contingency handling. When the spacecraft enters the lunar shadow region where solar-radiation pressure is unavailable, all solar-array deflection angles are returned to zero, solar-radiation-pressure-based unloading is temporarily disabled, and the reaction wheels maintain the spacecraft attitude independently. After exiting the shadow region, the solar-radiation-pressure torque model parameters are recalibrated, and the region-based unloading strategy is automatically resumed.

Step 6-3: Multi-orbit progressive momentum unloading. Due to the limited-magnitude but accurately controllable torque provided by the dual-eccentricity scheme, a multi-orbit staged dissipation strategy is adopted when the available unloading torque within a single orbit is insufficient. This strategy gradually dissipates the accumulated three-axis reaction-wheel momentum while maintaining power-generation efficiency and attitude stability.

Step 6-4: Periodic on-orbit parameter self-calibration. During the zero-momentum steady-state window of each draconic period, the equivalent three-axis control stiffness coefficients associated with the l_Y and l_Z eccentricities are recalibrated to compensate for solar-array optical degradation, thermal deformation, and small eccentricity drift. This process ensures long-term accuracy of the solar-radiation-pressure torque model.

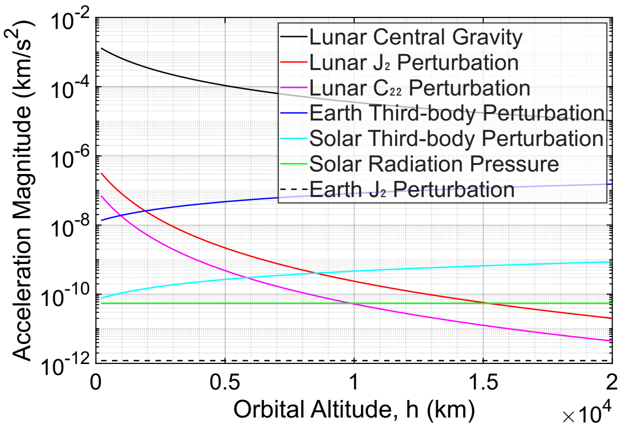

Fig. 2: Relative magnitudes of orbital perturbing accelerations in the lunar environment as a function of orbital altitude.

3.2 Orbit Prediction Analysis

Compared with the Earth environment, the lunar dynamical environment exhibits significant differences. In addition to the weaker central gravity of the Moon, the relative magnitudes of lunar J_2, C_{22} perturbations, solar-radiation-pressure perturbations, and Earth third-body perturbations vary with spacecraft orbital altitude, as illustrated in Fig. 2.

Assume that the spacecraft orbital altitude lies between 8000 and 10000 km. In this case, the perturbing acceleration induced by solar radiation pressure is approximately six orders of magnitude smaller than the lunar central gravitational acceleration. When the two solar arrays are rotated by small angles α, the increment of solar-radiation-pressure acceleration acting on the spacecraft can be approximated accordingly.

$$\Delta a_{\text{sun}} = \frac{\Delta F_{\text{sun}}}{m} = \frac{2P_0 S C_a (1 - \cos\alpha)}{m} \approx \frac{P_0 S C_a \alpha^2}{m}. \tag{29}$$

Here, m denotes the spacecraft mass. In engineering practice, typical values of the area-to-mass ratio and solar absorptivity are approximately $S/m = 0.01\,\text{m}^2/\text{kg}$ and $C_a = 0.85$, respectively. With a maximum deflection angle of $\alpha_{\max} = 0.1\,\text{rad}$, the corresponding solar-radiation-pressure-induced acceleration increment is approximately $\Delta a_{\text{sun}} = 3.88 \times 10^{-10}\,\text{m/s}^2$. Over one orbital period of approximately $86400\,\text{s}$, the resulting position error does not exceed $1.45\,\text{m}$. For lower lunar orbital altitudes, the position error induced by solar-radiation pressure becomes smaller due to the reduced disturbance accumulation over the shorter orbital period.

Table 2: Simulation parameters.

No.	Parameter	Value
1	Solar radiation pressure P_0	$4.56 \times 10^{-6}\,\mathrm{N/m^2}$
2	Single-array area S	$25\,\mathrm{m^2}$
3	$C_a/C_d/C_r$	$0.85/0.10/0.05$
4	Eccentric distance (l_Y, l_Z)	$2.0/0.30\,\mathrm{m}$
5	Orbital semimajor axis	$16700\,\mathrm{km}$
6	Orbital period	$53.794\,\mathrm{h}$
7	Simulation duration / step size	$60\,\mathrm{d}/60\,\mathrm{s}$
8	Long-period disturbance torque $(X/Y/Z)$	$2.0/0.35/2.0\,\mu\mathrm{N}\cdot\mathrm{m}$
9	Maximum deflection angle	$0.1\,\mathrm{rad}$
10	Activation threshold $(X/Y/Z)$	$0.50/0.20/0.50\,\mathrm{Nms}$
11	Exit threshold $(X/Y/Z)$	$0.10/0.05/0.10\,\mathrm{Nms}$

Table 3: Variation of reaction-wheel momentum with unloading.

Axis	Max without unloading (Nms)	Max with unloading (Nms)	Peak reduction	Dioscuri (Nms)
X	10.3827	0.8987	91.34%	0.7959
Y	1.8087	0.2000	88.94%	0.1216
Z	10.3722	1.2505	87.94%	1.1899

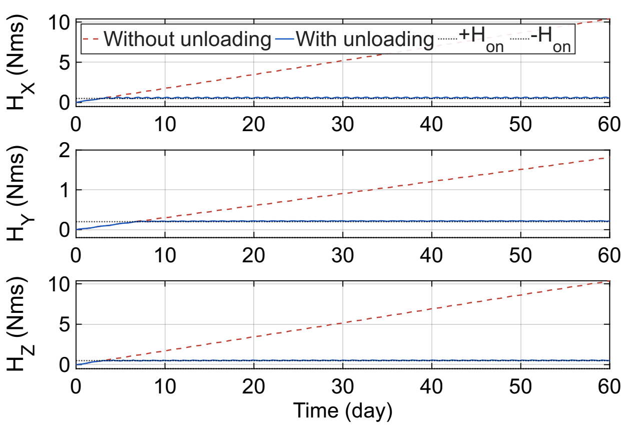

Fig. 3: Comparison of three-axis reaction-wheel momentum evolution with and without Dioscuri unloading.

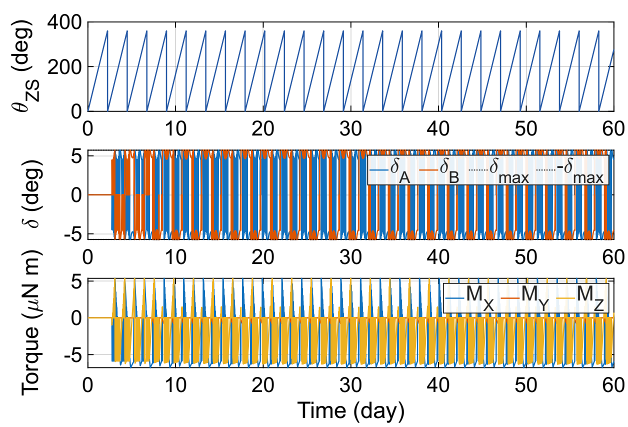

Fig. 4: Solar-vector geometry, dual-array deflection angles, and control torques during baseline unloading.

Compared with disturbance-torque unloading using thrusters, including Newton-level chemical thrusters and tens-of-millinewton electric thrusters, the relative thrust uncertainty is typically on the order of 1%–10%. The resulting acceleration error is approximately in the range of 10^{-5}–$10^{-6}\,\mathrm{m/s^2}$, which is several orders of magnitude larger than the acceleration disturbance introduced by solar-array-based unloading. Therefore, the proposed dual-solar-array unloading strategy not only reduces propellant consumption but also improves orbit-prediction accuracy.

4. Simulation Evaluation

Evaluations were carried out for a representative application scenario. The used simulation parameters are listed in Table 2.

The angle between the Sun direction and the spacecraft $+Z$-axis was divided into four regions over the range $0°$–

Table 4: System performance under different command holding times.

Holding time (min)	Num of mode switches	No accumulation	Max post-control momentum $[X, Y, Z]$/(Nms)
600	416	No	$[0.6221,\ 0.2220,\ 0.6384]$
590	416	No	$[0.6196,\ 0.2212,\ 0.6324]$
580	446	Yes	$[0.6170,\ 0.2206,\ 0.6259]$
570	507	Yes	$[0.6396,\ 0.2274,\ 0.6306]$
560	532	Yes	$[0.6187,\ 0.2204,\ 0.6170]$
550	656	Yes	$[0.6218,\ 0.2201,\ 0.6085]$
540	753	Yes	$[0.6232,\ 0.2202,\ 0.6094]$

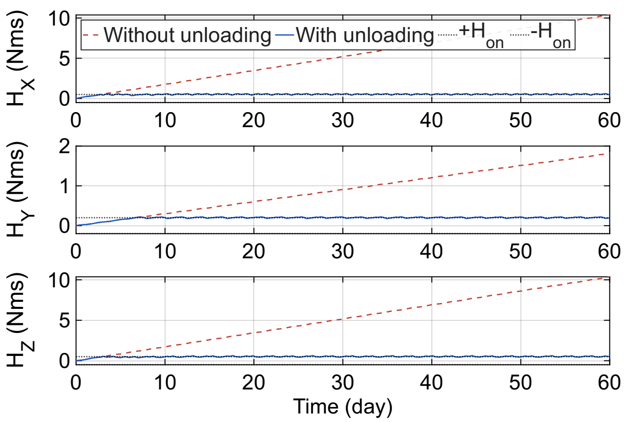

Fig. 5: Reaction-wheel momentum comparison with and without unloading under the optimized command holding time.

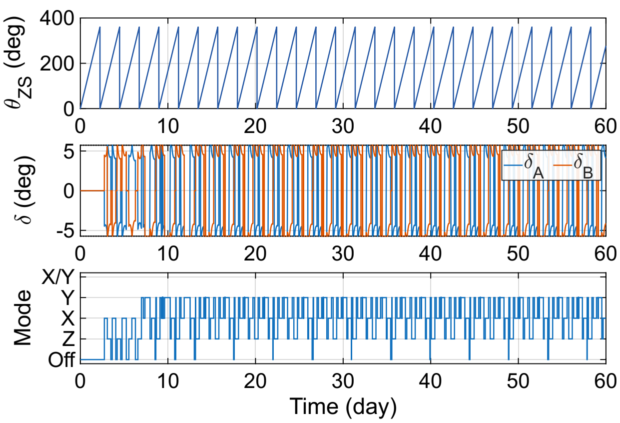

Fig. 6: Solar-vector geometry, dual-array deflection commands, and control-mode switching under the optimized holding time.

360°. In Regions I and III, Group G1 differential deflection was preferentially used for Z-axis unloading. In Regions II and IV, Group G2 differential deflection was preferentially used for X-axis unloading, whereas Group G3 common-mode deflection was used for Y-axis unloading according to the available control gain. The control commands of Groups G2 and G3 could be superposed. A hysteresis criterion was adopted by the controller, and the target torque consisted of long-period disturbance-torque feedforward and proportional feedback of wheel momentum. After command synthesis for the two arrays, uniform scaling was applied to ensure that the deflection of either array did not exceed 0.1 rad. The command holding time was set to 30 min.

The simulation results of the reaction-wheel momentum after unloading are summarized in Table 3. Fig. 3 compares the reaction-wheel momentum histories with and without unloading, and Fig. 4 presents the solar azimuth, array deflection angles, and control torques.

During the simulation, the maximum solar-array deflection angle reached the preset saturation limit of $5.730°$, and the deflection angle frequently operated near this upper bound. The corresponding control duty cycle was 95.43%, indicating that the available control margin was limited for the selected solar-array area and eccentric lever arm. The maximum unloading torques generated about the X-, Y-, and Z-axes were $7.60\,\mu\mathrm{N}\cdot\mathrm{m}$, $0.831\,\mu\mathrm{N}\cdot\mathrm{m}$, and $6.13\,\mu\mathrm{N}\cdot\mathrm{m}$, respectively.

Without unloading, the long-period disturbance torque caused continuous accumulation of angular momentum along all three axes. After enabling dual-solar-array unloading, the peak momentum values of the X-, Y-, and Z-axes were reduced by 91.34%, 88.94%, and 87.94%, respectively, demonstrating that the region-based differential/common-mode control strategy can significantly suppress the growth of reaction-wheel momentum.

Periodic fluctuations appeared in the X- and Z-axis momentum at region-switching instants because differential deflection can provide high control gain for either the X- or the Z-axis at a given time, depending on the solar direction. The higher peak value observed on the Z-axis results from a less favorable phase relationship between its unloading window and the disturbance-torque phase.

To reduce the frequency of solar-array deflection maneuvers and identify the longest holding time that still maintains effective unloading, simulations were carried out for different command holding times, as listed in Table 4.

It can be seen that when the holding time is 580 min, continuous accumulation of three-axis momentum can still be prevented while the number of solar-array control mode switches is minimized. The comparative simulation results of angular momentum with and without unloading are shown in Fig. 5, and the solar azimuth, dual-array deflection angles, and mode switching results are shown in Fig. 6.

The number of mode switches decreases to 446, the control duty cycle is 92%, and the maximum deflection-angle saturation ratio is 48.6%. After momentum unloading, the peak momentum values of the X-, Y-, and Z-axes are reduced by 94.06%, 87.80%, and 93.97%, respectively. No statistically significant long-term positive linear growth term remains on any of the three axes.

5. Conclusion

This paper investigates disturbance torque unloading for lunar-orbiting satellites equipped with zero-momentum attitude control systems, where conventional magnetic torquers are unavailable. A novel unloading approach based on conventional dual solar arrays is proposed. An analytical torque model is established, an on-orbit implementation strategy is developed, the impact of solar-array-based unloading on orbit-prediction accuracy is analyzed, and representative mission scenarios are evaluated through simulations.

The results demonstrate that by introducing a preset eccentricity along the spacecraft Z-direction during solar-array installation, the two solar arrays can generate controllable torques through region-dependent small-angle anti-phase and in-phase deflections, enabling three-axis disturbance torque unloading without additional auxiliary flaps. For the considered attitude configuration with the spacecraft Y-axis perpendicular to the ecliptic plane and the X-axis aligned with the flight direction, the orbital cycle is divided into four regions according to the solar-vector geometry. Anti-phase deflection in Regions I and III enables decoupled Z-axis momentum unloading, while coordinated anti-phase and in-phase deflections in Regions II and IV enable decoupled X- and Y-axis momentum unloading. Consequently, three-axis momentum unloading can be achieved through a unified dual-solar-array control framework.

From an engineering implementation perspective, extending the holding duration of each unloading action can improve the efficiency of the proposed method. For high lunar orbits with relatively large solar-array areas, a single control action can maintain an effective unloading effect for up to approximately 580 min, while suppressing continuous momentum accumulation and maintaining the system near the zero-momentum operating state.

The orbit-prediction analysis further shows that when the solar-array deflection angle is limited within 0.1 rad, the additional acceleration perturbation introduced by solar-radiation-pressure-based unloading is significantly smaller than the residual acceleration errors associated with thruster-based unloading. Therefore, the proposed method can achieve reaction-wheel momentum unloading while reducing the impact on orbit prediction and avoiding additional propellant consumption.

This work provides an alternative momentum unloading approach for lunar-orbiting spacecraft and a feasible implementation framework using conventional dual solar arrays. Nevertheless, several challenges remain, including the complexity of the hysteresis-based control logic, the relatively frequent solar-array operations, and the reduced efficiency when multiple axes are simultaneously controlled in Regions II and IV. Future work will investigate simplified switching control strategies and extend the analysis to alternative attitude configurations with the spacecraft $+Z$-axis pointing toward the lunar center.

References

[1] Angie Bukley and Colleen Stover. Moonstruck! international aspirations in cislunar space. *Space Agenda*, pages 2024–10, 2025.

[2] Yingzhuo Jia, Yongliao Zou, Jinsong Ping, Changbin Xue, Jun Yan, and Yuanming Ning. The scientific objectives and payloads of Chang'E-4 mission. *Planetary and Space Science*, 162:207–215, 2018. Lunar Reconnaissance Orbiter – Seven Years of Exploration and Discovery.

[3] Marshall Smith, Douglas Craig, Nicole Herrmann, Erin Mahoney, Jonathan Krezel, Nate McIntyre, and Kandyce Goodliff. The Artemis Program: An Overview of NASA's Activities to Return Humans to the Moon. In *2020 IEEE Aerospace Conference*, pages 1–10, 2020.

[4] L. J. Wittenberg, E. N. Cameron, G. L. Kulcinski, S. H. Ott, J. F. Santarius, G. I. Sviatoslavsky, I. N. SViatoslavsky, and H. E. Thompson. A review of 3he resources and acquisition for use as fusion fuel. *Fusion Technology*, 21(4):2230–2253, 1992.

[5] C. I. Honniball, P. G. Lucey, S. Li, S. Shenoy, T. M. Orlando, C. A. Hibbitts, D. M. Hurley, and W. M. Farrell. Molecular water detected on the sunlit moon by SOFIA. *Nature Astronomy*, 5(2):121–127, 2021.

[6] Peng Zhang, Wei Dai, Ran Niu, Guang Zhang, Guanghui Liu, Xin Liu, Zheng Bo, Zhi Wang, Haibo Zheng, Chengbao Liu, Hanzhe Yang, Yifan Bai, Yang Zhang, Dong Yan, Kefa Zhou, and Ming Gao. Overview of the lunar in situ resource utilization techniques for future lunar missions. *Space: Science & Technology*, 3:0037, 2023.

[7] Norman F. Ness. The Magnetic Fields of Mercury, Mars, and Moon. *Annual Review of Earth and Planetary Sciences*, 7:249–288, 1979.

[8] J.S. Halekas, Y. Saito, G.T. Delory, and W.M. Farrell. New views of the lunar plasma environment. *Planetary and Space Science*, 59(14):1681–1694, 2011. Lunar Dust, Atmosphere and Plasma: The Next Steps.

[9] Yun Liu and Yangting Lin. Key scientific questions for future lunar exploration. *Space: Science & Technology*, 4:0241, 2024.

[10] Steve Creech, John Guidi, and Darcy Elburn. Artemis: An Overview of NASA's Activities to Return Humans to the Moon. In *2022 IEEE Aerospace Conference (AERO)*, pages 1–7, 2022.

[11] V. Angelopoulos. The ARTEMIS Mission. *Space Science Reviews*, 165(1):3–25, December 2011.

[12] Chunlai Li, Jianjun Liu, Xin Ren, Wei Zuo, Xu Tan, Weibin Wen, Han Li, Lingli Mu, Yan Su, Hongbo Zhang, Jun Yan, and Ziyuan Ouyang. The Chang'e 3 Mission Overview. *Space Science Reviews*, 190(1):85–101, July 2015.

[13] Weiren Wu, Dengyun Yu, Chi Wang, Jizhong Liu, Yuhua Tang, He Zhang, and Zhe Zhang. Technological Breakthroughs and Scientific Progress of the Chang'e-4 Mission. *Science China Information Sciences*, 63(10):200201, September 2020.

[14] Geunho Song. An analysis of lunar exploration competition in the new space era and recommendations for korea's space exploration program. *The Korean Journal of Security Affairs*, 30(1):53–73, 2025.

[15] Mark Flanegan, Jonathon Gal-Edd, Lynn Anderson, Joseph Warner, Todd Ely, Charles Lee, Biren Shah, Arvydas Vaisnys, and James Schier. *NASA Lunar Communication and Navigation Architecture*.

[16] Shaojun Bi, Changgang Zheng, Congwei Yang, Jinjun Zheng, Chengyan He, and Jiaxing Liu. In-orbit Experimental of Satellite-induced Code Pseudorange Deviations of BeiDou System. In *Proceedings of the 31st International Technical Meeting of the Satellite Division of the Institute of Navigation (ION GNSS+ 2018)*, pages 1257–1267, Miami, Florida, USA, September 2018. Institute of Navigation.

[17] Xiao Tao, Wei Ding, Shuo Wang, Xingang Zhang, Wanzhao Cui, and Qinglong Cui. An Active Multi-Beam Antenna Design Method and Its Application for the Future 6G Satellite Network. *Space: Science & Technology*, 4:0149, July 2024.

[18] J. Lievre. Solar sailing attitude control of large geostationary satellite. *IFAC Proceedings Volumes*, 18(4):29–32, 1985. 10th IFAC Symposium on Automatic Control in Space 1985, Toulouse, France, 24-28 June.

[19] Yue Xu, Ming Jiang, Mingyang Zhu, Nan Hu, Chunming Zhao, and Jiangzhou Wang. Reduced-Complexity Decoding of 3D Product Codes for Satellite Communications. *Space: Science & Technology*, 4(0096):0096, 2024.

[20] Ruth Azor. Solar attitude control including active nutation damping in a fixed-momentum wheel satellite. In *Guidance, Navigation and Control Conference*, pages 226–235, August 1992.